



Reduced graphene oxide/TiO₂ nanotube composites for formic acid photodegradation



M. Hamandi ^{a,b}, G. Berhault ^{b,*}, C. Guillard ^b, H. Kochkar ^{a,c,**}

^a Université de Tunis El Manar, Faculté des Sciences de Tunis, Laboratoire de Chimie des Matériaux et Catalyse, 2092 Tunis, Tunisia

^b Institut de Recherches sur la Catalyse et l'Environnement de Lyon, IRECLYON, CNRS, University of Lyon I, Villeurbanne 69100, France

^c Laboratoire de Valorisation des Matériaux Utiles, Centre National de Recherches en Sciences des Matériaux (CNRSM), Technopôle Borj-Cedria, 8027 Soliman, Tunisia

ARTICLE INFO

Article history:

Received 17 November 2016

Received in revised form 12 February 2017

Accepted 18 February 2017

Available online 21 February 2017

Keywords:

Graphene oxide

TiO₂ nanotubes

Photocatalysis

Formic acid

ABSTRACT

The influence on the photocatalytic performance of TiO₂ nanotubes (NT) resulting from the addition of graphene oxide (GO) was studied. TiO₂ nanotubes (NT) were prepared using alkaline hydrothermal treatment of TiO₂ P25 followed by calcination at 400 °C under air. GO-NT composites were then obtained by wet impregnation of the as-prepared TiO₂ nanotubes onto graphene oxide before reduction under H₂ at 200 °C. In a first step, the influence of the reduction treatment was evaluated on GO alone to determine its role towards the nature of the oxygen-containing functional groups present. GO-NT composites were also characterized considering both the effect of the reduction treatment and of the GO weight loading on textural, structural, electronic, and optical properties of TiO₂ nanotubes. The resulting GO-NT composites were finally evaluated for the photocatalytic degradation of formic acid and compared to TiO₂ nanotubes alone and to P25. Results emphasize a strong increase of the electron affinity and conductivity of the GO-NT composites if graphene oxide is reduced at 200 °C. These enhanced properties lead to an easier separation of photogenerated charges and to a limitation of the recombination of electron-hole pairs. A dramatic gain in photocatalytic response is observed. Maximum in photocatalytic efficiency is reached at a GO loading of 1.0 wt% while further increase of GO weight loading blocks light penetration and depletes the photocatalytic response.

© 2017 Elsevier B.V. All rights reserved.

1. Introduction

Photocatalysis is considered as an efficient advanced oxidation process (AOPs) for the degradation of toxic molecules [1]. Under UV illumination, TiO₂ could produce powerful oxidants capable to degrade organic pollutants until total mineralization [2,3]. However, TiO₂ presents a high recombination rate of the photo-generated electron-hole pairs lowering its photocatalytic activity. In order to overcome this limitation, many studies have been carried out to improve the photocatalytic activity of TiO₂ by depositing C-allotropes such as graphene. Graphene has become one of the most exciting materials over the past few years and continues to receive important attention. This interest has extended to the field of photocatalysis for both the degradation of dyes and the conver-

sion of carbon dioxide [4–8]. Many studies questioned whether or not graphene can be considered a good electron acceptor (trap) able to enhance photocatalytic properties [9,10]. Recently, several studies showed that decorating semiconductor materials with graphene could considerably enhance their electronic [11], photo-electronic [12], electrocatalytic [13] and photocatalytic properties [14–16]. For instance, the recombination rate between electrons and holes would decrease in the presence of graphene because its high electronic conductivity would lead to an easier transportation and separation of photogenerated charges [17–20]. However, other factors like the defect density, the doping by N or B heteroatoms, the interfacial contact between graphene and the semiconductor or the dimensionality of graphene (dots, nanoribbons, 3D frameworks) can influence the photocatalytic performance [21–23].

Decorating TiO₂ with graphene or graphene oxide has been studied extensively for the photodegradation of dyes [5,18,24]. Many strategies for improving photocatalytic activity of graphene/TiO₂ composites have been envisaged such as the assistance of anionic sulfate surfactants, minimization of graphene defects, and formation of heterojunctions and/or optimization of

* Corresponding author.

** Corresponding author at: Université de Tunis El Manar, Faculté des Sciences de Tunis, Laboratoire de Chimie des Matériaux et Catalyse, 2092 Tunis, Tunisia.

E-mail addresses: gilles.berhault@ircelyon.univ-lyon1.fr (G. Berhault), h.kochkar@yahoo.fr (H. Kochkar).

the graphene content [7,16,25]. These previous studies concluded that the enhancement of photocatalytic activity is due to a better separation of electron-hole pairs but without providing further clarification. However, the current studies often lack the correlation between graphene properties and the photocatalytic performance of the graphene/TiO₂ composite.

Research about graphene/TiO₂ nanotube composites was scarcely envisaged. Indeed, even if many studies were performed about the preparation of graphene/TiO₂ photocatalysts, combination of graphene and nanotubular TiO₂ was rarely investigated [5,26]. Moreover, to our knowledge, the graphene/TiO₂ nanotube composite was not envisaged for degrading pollutants other than dyes. This is surprising since, in contrast to TiO₂ nanoparticles and nanorods, TiO₂ nanotubes have much higher surface area with a higher number of active sites. Therefore, a greater degree of interfacial contact associated with the interface between TiO₂ nanotubes and graphene should favor charge separation. In previous studies, the superiority of nanotubular TiO₂ over spherical nanoparticles was clearly observed for both the degradation of formic acid [27,28] as well as for the inactivation of pathogens [29]. In particular, the nanotubular morphology was found to restrict the anatase crystallite size while maintaining high surface area limiting electron-hole bulk recombination.

The aim of the present work will then consist in the development of a facile method for the elaboration of graphene oxide/TiO₂ nanotube (GO-NT) composites by controlling the GO content and its reduction degree. Indeed, the GO content is known to strongly influence the photocatalytic response of semiconductors [30,31]. Moreover, increasing the amount of oxygenated groups present on GO can widen the graphene bandgap with an upshift of its conduction band [32]. Similarly, size, shape, and morphology of GO can influence the photocatalytic properties of GO-TiO₂ composites [33,34].

The photocatalytic activity of these composites will be evaluated in the photodegradation of formic acid under UV light irradiation. Formic acid has been chosen here because its photodegradation leads only to CO₂ and H₂O without forming any other stable intermediate [35,36]. The photocatalytic degradation of formic acid into CO₂ is also the final step in the decomposition of many complex organic compounds under photocatalytic conditions.

2. Experimental

2.1. Elaboration of graphene oxide

Graphene oxide (GO) was elaborated by oxidation of natural graphite according to an improved Hummer's method [37,38]. 70 mL of concentrated H₂SO₄/H₃PO₄ (9:1 v/v) were first stirred with 3.0 g of graphite in an ice bath. Then, 9.0 g of KMnO₄ were added slowly while keeping the temperature of the suspension lower than 20 °C. The solution was then transferred to an oil bath and was kept stirring for ½ h. 150 mL of water were added and the solution was further stirred for 15 min more at 40 °C. 500 mL of water were added again followed by a slow addition of 15 mL of H₂O₂ (35%). The resulting solution was filtered before being washed with 250 mL of hydrochloric acid (1:10) in order to remove metallic ions. The as-formed graphite oxide solid was diluted to 600 mL. The dispersion was purified from metallic species by dialysis for 7 days (membrane with cut off molecular weight: 8000–14,000 g mol⁻¹). The graphite oxide dispersion was sonicated for 6 h before being stirred for 12 h to exfoliate it into graphene oxide (GO). The dispersion was centrifuged at 10000 rpm for ½ h to eliminate the remaining non-exfoliated graphite oxide.

2.2. Elaboration of TiO₂ nanotubes

TiO₂ nanotubes were elaborated via alkaline hydrothermal treatment. 3.0 g of TiO₂ P25 (80% anatase, 20% rutile) were first transferred with 90 mL of NaOH (11.25 mol L⁻¹) to a 150 mL Teflon-lined autoclave. Hydrothermal treatment was performed at 130 °C for 20 h. The as-formed titanate material was washed with deionized water and HCl (0.1 mol L⁻¹) until the final rinsing solution shows a pH value of 6.5. The solid was dried at 80 °C for 1 day. For complete sodium elimination, a second washing step was carried out using a 1.0 M HCl solution. The solid was calcined at 400 °C under O₂ (heating rate: 2 °C·min⁻¹) to obtain anatase nanotubes (NT).

2.3. Elaboration of GO-NT composites

Graphene oxide was added to TiO₂ nanotubes with different weight loadings going from 0.5 to 5.0 wt% using an incipient wetness impregnation. The mixture was dried at 80 °C for 24 h and finally reduced under H₂ at 200 °C for 2 h. The composites are named x%GO-NT-T where x is the weight loading in GO and T is the reduction temperature in °C.

2.4. Characterization

Nitrogen physisorption measurements at 77 K were carried out using a Micromeritics ASAP 2020 instrument. The Brunauer-Emmett-Teller (BET) method was used to determine the specific surface areas using the adsorption data branch in the relative P/P₀ pressure range going from 0.05 to 0.25. The Barrett-Joyner-Halenda (BJH) model was used to obtain pore size distributions.

X-ray Diffraction (XRD) analyses were performed using a Bruker D8 Advance A25 diffractometer with Cu K α radiation ($\lambda = 1.54184 \text{ \AA}$). Crystallite sizes were obtained using the Scherrer equation:

$$L = K\lambda/\beta\cos\theta$$

where L is the crystallite size, λ is the wavelength of X-ray radiation, β is the full width at half-maximum, and K the shape factor taken as 1.

Raman experiments were performed at 20 °C from 100 to 2500 cm⁻¹ using a Horiba Jobin Yvon LabRAM-HR equipment. A spectral resolution of 4 cm⁻¹ was achieved while a 514 nm Ar-Kr RM2018 laser and a CCD detector cooled at -75 °C were used. The average power at the solid surface was set at 1 mW.

Transmission Electron Microscopy (TEM) was performed on a JEOL 2010 (200 kV) microscope to reveal the morphology of the different samples. The TEM analysis specimens were first dispersed in ethanol before dropwise addition and drying onto a holey carbon film supported on a Cu grid (300 mesh).

UV-vis diffuse reflectance spectroscopy (UV-vis DRS) measurements were performed using an AvaSpec-2048 Fiber Optic Spectrometer with a symmetrical Czerny-Turner design. Spectra were recorded from 250 to 800 nm using a 2048 pixel CCD detector array. Band gap energy values were evaluated using the Kubelka-Munk method: F(R)h $\nu^{1/2}$ versus h ν plots were built with F(R) = (1-R)/2R assuming an indirect band gap transition.

Fourier transform infrared (FTIR) spectra were recorded from 4000 to 400 cm⁻¹ on a Perkin Elmer (Spectrum BX) spectrometer (spectral resolution of 4 cm⁻¹, accumulation of 100 scans).

The photoluminescence (PL) analysis was performed using a PerkinElmer LS55 spectrofluorophotometer equipped with a Xe lamp presenting an excited wavelength at 330 nm.

X-ray photoelectron spectroscopy (XPS) studies were carried out using a KRATOS Axis Ultra spectrometer equipped with a dual

Al/Mg anode and a hemi-spherical analyzer operating at fixed pass energy of 40 eV. A 150 W monochromatic source (Al K α = 1486.6 eV) was used. The samples were pressed on an indium foil attached to the sample holder and placed into the XPS instrument. Binding energies were obtained with a precision of ± 0.2 eV. Curve fitting was done using mixed Gaussian and Lorentzian functions for line shaping after treatment of the background using a Shirley type baseline (casaXPS software, version 2.0.71). UV photoelectron spectroscopy (UPS) was performed applying the same instrument as XPS, using a He-I source (21.2 eV). Samples were fixed on indium tin oxide (ITO) blades.

The photocurrent and impedance measurements were carried out using a MetrohmAutolab instrument. The electrochemical system consists of three electrodes using a GO-TiO₂ modified glassy ITO electrode, a platinum wire counter electrode and a saturated calomel reference electrode (SCE). All potentials are quoted versus SCE. Sodium sulfate with a concentration of 0.5 M was used as electrolytic solution. For photocurrent experiments, a Xenon lamp (500 W) providing maximum energy at 365 nm was used as UV source. The distance between the bottom of the reactor and the UV source was adjusted in order to maintain a radiant flux of 5 mW min⁻¹ (as measured with a VLX-3W radiometer equipped with a CX-365 detector (UV-A)).

2.5. Photocatalytic experiments

Photocatalytic tests were performed using an aqueous solution (30 cm³) containing different concentrations of formic acid as the reactant molecule to be degraded. Reaction was carried out in a Pyrex photoreactor (100 cm³) (optical window area: 12.5 cm²). The concentration of photocatalyst was set at 1.0 g L⁻¹ for all the samples studied. The pH of the different solutions was close to 3.0 ± 0.5 depending on the formic acid concentration used. A high-pressure Philips HPK 125 W Hg lamp was used for UV irradiation (maximum energy at 365 nm). An optical Corning filter 0.52 was employed to cut-off wavelength below 340 nm. A radiant flux of 5 mW min⁻¹ was fixed for all experiments. Before UV irradiation, the suspensions were stirred at a given formic acid concentration in the dark for 30 min to reach adsorption equilibrium conditions. The formic acid concentration of the solution after equilibration was measured and used as the initial concentration (C_0). Formic acid samples were taken for analysis at different intervals (C) from the photoreactor while the photocatalyst was separated from the liquid phase by filtration. The samples withdrawn were analyzed with a Varian ProStar High Performance Liquid Chromatograph (HPLC) equipped with a Coregel-87H3 column (300 mm \times 7.8 mm). A H₂SO₄ (5.10⁻³ mol L⁻¹) mobile phase was used at a flow rate of 0.7 mL min⁻¹.

3. Results and discussion

3.1. Characterization of graphene oxide

Based on XRD analysis (Fig. S1, Supplementary information), the starting graphite material appears well crystallized and presents only one intense characteristic diffraction peak at 26.5° (interlayer spacing: 3.4 Å) corresponding to the C(002) plane [39]. After oxidation using the modified Hummer's method, the graphitic peak completely disappears while a new peak at $2\theta = 10.8^\circ$ (interlayer spacing: 8.3 Å) emerges as well as a broad signal around 23°. This result confirms the successful oxidation of graphite into graphene oxide [40]. The graphene oxide sample reduced at 200 °C under H₂ shows the disappearance of the diffraction peak of graphite oxide at $2\theta = 10.8^\circ$ while only a broad peak is now found at 26.5° as expected for reduced graphene oxide samples [39].

The functional groups present in GO are known to correspond to hydroxyl and epoxy groups on its basal planes and to carboxyl groups at the edges [41]. The amount of these functional groups can be controlled by chemical or thermal treatments. Fig. 1 presents the FTIR spectra of graphite and graphene oxide before and after reduction. The spectrum of GO presents typical modes related to different oxygen-containing functional groups [42,43]. For instance, carboxyl groups present contributions at 1410 and 1720 cm⁻¹ corresponding to C—OH and C=O stretching vibrations respectively. Additionally, a shoulder at 3220 cm⁻¹ corresponds to O—H vibrations of carboxyl groups. Epoxy groups exhibit vibrational bands at 1100 and 1160 cm⁻¹ corresponding to C—O stretching vibration and to C—O—C breathing mode respectively. Finally, hydroxyl groups contribute through a broad O—H vibration centered at 3420 cm⁻¹. Other bands can be noticed at 1640 cm⁻¹ (in plane C=C stretching) and at 2850 and 2920 cm⁻¹ (C—H stretching vibrations respectively of sp³ and sp² species).

After reduction, the intensities of the different oxygen-containing functional groups drastically decrease. However, they do not disappear completely showing that reduction at 200 °C leads to the persistence of some oxygen-containing groups. This is confirmed by elemental analysis results. Indeed, GO contains 45.9 wt% of oxygen, 2.6 wt% of hydrogen and 51.5 wt% of carbon. However, GO reduced at 200 °C still contains 3.7 wt% of oxygen in plus of 1.0 wt% of hydrogen and 95.3 wt% of carbon.

Raman spectra of graphite and graphene oxide before and after reduction at 200 °C are presented in Fig. 2. Two main contributions can be noticed. The first one corresponds to the so-called G band originating from the in-plane vibration of sp² carbon atoms observed for all samples. The second D band observed mainly on graphene oxide is a defect-activated breathing mode with A_{1g} symmetry. A more detailed analysis of the Raman spectra shows that graphite presents an intense characteristic G band with only a quite weak D contribution indicating the presence of only few defects on this sample. Moreover, the G band arises at 1584 cm⁻¹ in agreement with the value reported for crystalline graphite [44,45]. Graphene oxide samples before and after reduction at 200 °C present a broad asymmetric G band characteristic of disordered graphite rather than pristine graphite oxide [46]. Compared to graphite oxide, graphene oxide presents a shift to 1598 cm⁻¹ before reduction and to 1600 cm⁻¹ after reduction. This shift results from the overlap between the G mode and the higher frequency defect activated D' band (~1620 cm⁻¹) characteristic of disordered graphite samples [47,48]. Moreover, the strong D contribution of graphene oxide shifts from 1362 cm⁻¹ to 1389 cm⁻¹ after reduction.

The D/G intensity ratio (I_D/I_G) is generally considered to be an indication of disorder in GO originating from defects associated with vacancies, grain boundaries, and amorphous carbon [49]. The I_D/I_G ratio decreases from 0.82 to 0.79 (Table 1) after reduction of graphene oxide in agreement with a lower amount of defects on the reduced sample consecutively to the removal of oxygen-containing functional groups.

The type and amount of functional groups of GO and GOR-200 were determined by XPS (Table 1 and Fig. 3). Three different contributions can be noticed at 284.6 eV due to non-oxygenated C=C bonds, at 286.5 eV due to C—O bonds (hydroxyls attached to graphene or epoxy groups) and at 288.3 eV due to carboxylate carbon [50]. Results clearly emphasize that the reduction of graphene oxide at 200 °C is not complete. However, the reduction efficiency also depends strongly on the nature of the oxygen-containing groups. While the C—O contribution due to hydroxyl or epoxy groups decreases from 51 to 25%, the carboxylate proportion, even if much lower, remains the same at 8–9%. This result is in agreement with Kim et al. [51] showing a greater stability of carboxylic groups at the edges of graphene layers. It should also be noted a shift from 286.5 eV to 285.8 eV of the C—O contribution suggesting the persis-

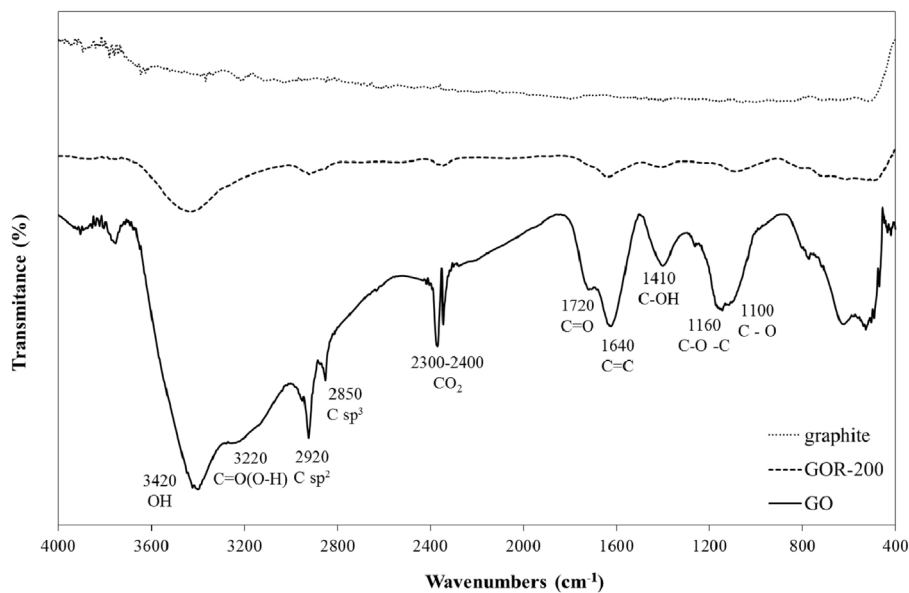


Fig. 1. FTIR spectra of graphite, graphene oxide (GO), and graphene oxide reduced at 200 °C (GOR-200).

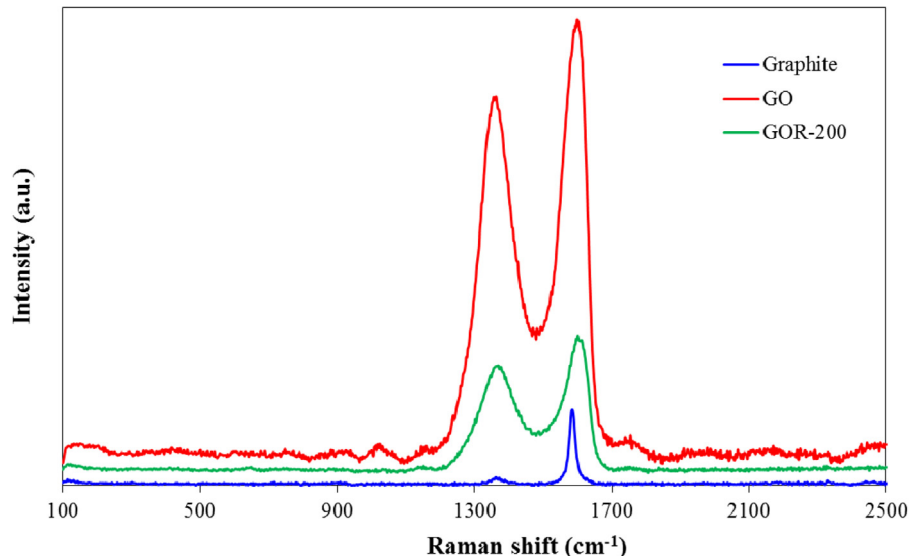


Fig. 2. Raman spectra of graphite, graphene oxide (GO), and graphene oxide reduced at 200 °C (GOR-200).

Table 1

Structural properties of graphite and graphene oxide before and after reduction as determined by XPS, UPS, and Raman. XPS results show the decomposition of C1s core-level spectra into three contributions corresponding to non-oxygenated C=C, C—O bonds (arising from hydroxyls or epoxy groups), and C=O bonds from carboxylic groups. Work functions were determined by UPS. Finally, Raman results indicate the position of the D and G bands and their relative intensity ratios.

| Samples | XPS | | | | UPS | Raman | | |
|----------|---------|---------|------------|---------------|-----|--------------------------------|------------------------------------|------------------------------------|
| | C—C (%) | C—O (%) | C(O)OH (%) | C—O/C—C (wt.) | | I _D /I _G | W _D (cm ⁻¹) | W _G (cm ⁻¹) |
| graphite | 100 | — | — | — | 4.4 | 0.09 | 1360 | 1584 |
| GO | 41 | 51 | 8 | 1.2 | 4.6 | 0.82 | 1362 | 1598 |
| GOR-200 | 66 | 25 | 9 | 0.4 | 4.1 | 0.79 | 1369 | 1600 |

tence of some hydroxyl groups probably by hydrogenation of epoxy moieties instead of their removal. In addition, the reduction process not only caused the elimination of oxygen-containing functional groups but also it leads to a rearrangement of the graphene structure. The reduction at 200 °C allows a restoration of the sp² bonded C atoms as confirmed by XPS since the graphene oxide shows an increase of the C=C proportion from 41 to 66% after reduction. This restoration can affect directly the conductivity of GO. Despite the

fact that graphene oxide is a semiconductor, its electronic properties are tunable and can be controlled by varying the reduction degree. Thus, it could be transformed from a semiconductor to a conductor by a simple reduction.

To study this interesting property, UPS was carried out on graphite and on graphene oxide before and after reduction. UPS is highly surface sensitive and is ideal to study adsorbed molecular monolayers on surfaces like graphene oxide. As the UPS source

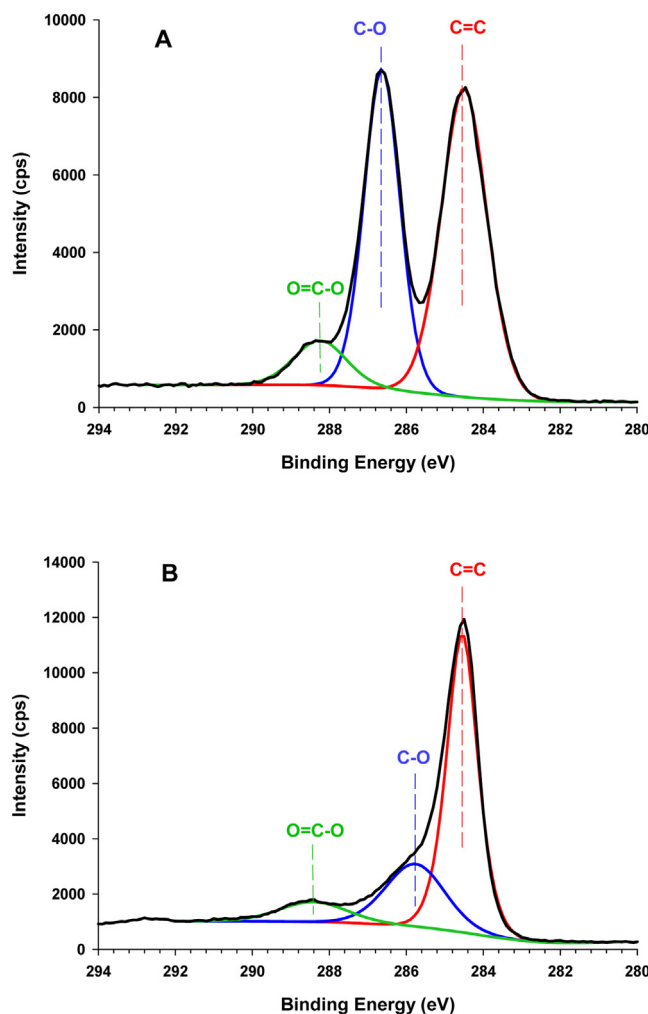


Fig. 3. C1s XPS spectra of GO (A) and GOR-200 (B).

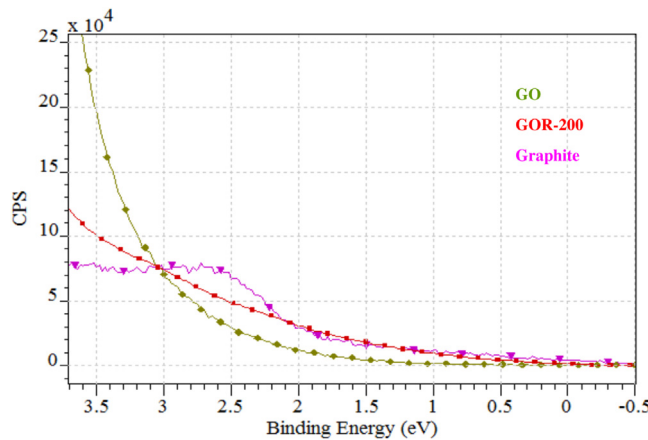


Fig. 4. He-I UPS valence band spectra near the Fermi level of graphite, graphene oxide (GO), and graphene oxide reduced at 200 °C (GOR-200).

excites only valence bond electrons, information about the distribution of electrons in the valence band and the densities of states near the Fermi level are provided. Valence band spectra obtained by He-I UPS measurements on graphene oxide before and after reduction as well as on graphite are presented in Fig. 4. The Fermi level position is referred at a binding energy of 0 eV. All the spectra are dominated by a broad band centered at ~8 eV

but differ at low energy with features centered at ~2.5–3.0 eV. These features decrease in intensity when going from graphite to reduced graphene oxide and finally graphene oxide. This is in agreement with an increase in C2p- π states as a result of the increase in graphitic carbon content or the decrease in surface functional groups upon reduction [52]. Fig. 4 also indicates a steep increase of the density of states near the Fermi level after reduction of graphene oxide. This result is in agreement with an increase in conductivity in the case of reduced graphene oxide [38]. In the low kinetic energy regime, the secondary electron cut-off energy depends on the work function of the material. The electron affinity was deduced by measuring the work function (Table 1). The work function of graphene oxide at ~4.6 eV decreases to ~4.1 eV after reduction in agreement with Adan-Mas et al. [53]. Moreover, considering that the band gap of graphene oxide is expected around 1.8–2.1 eV [54], the valence band would be observed between –6.4 and –6.7 eV (in absolute vacuum scale). In the case of graphite, the work function was measured at 4.4 eV also in agreement with the literature value [55]. The higher work function observed in the case of GO possibly results from the presence of surface dipole moments attributable to the oxygen functional groups which disrupt π conjugation [49]. Also, it is worth noting that there is no significant shift in the peak position of the C=C component of C1s XPS spectrum of reduced graphene oxide as compared to graphene oxide. Therefore, the Fermi level position is not shifted while the vacuum level shifts downward through removal of surface dipoles causing the decrease of the work function. Thus, the heterogeneous electronic structure of graphene oxide comprises a variety of electronic states originating from different configurations of sp² and sp³ hybridized carbon atoms whose relative fractions are controlled by the degree of reduction [56]. These modifications caused by the reduction step can influence the properties of hybridized GO-NT composites.

3.2. Characterization of GO-NT composites

The textural properties of the GO-NT composites were first studied. The theoretical specific surface area value for fully exfoliated graphene material is around 2600 m² g⁻¹ [57]. The addition of GO to TiO₂ nanotubes would then be expected to increase the specific surface area of the nanocomposites. However, as shown in Table 2, specific surface areas in fact decrease when GO (reduced or not) is added to TiO₂ nanotubes. These values are therefore much lower than those expected theoretically. This marked discrepancy is considered to arise from the restacking and strong interaction of graphene layers when they are dried, differing substantially from the area of the macrosheets present in the colloidal suspension [58]. Finally, comparison between GO-NT and GO-NT-200 composites shows that the reduction of graphene does not influence significantly the specific surface areas. Moreover, increasing the GO or GO-200 loading leads first to a decrease (from 1.0 to 3.0 wt% GO) then to a slight increase in surface area (at 5.0 wt% GO). Pore size values show a maximum at 1.0 wt% GO before decreasing for higher GO loading. Once again, the reduction of graphene oxide does not impact the porosity.

XRD patterns of the TiO₂ nanotubes and of the GO-NT composites before and after reduction at 200 °C were recorded for GO loadings going from 1.0 to 5.0 wt% (Fig. S2, Supplementary Information). All the patterns exhibit the same characteristic (101), (103), (200), (105), (211), (118) and (116) reflections corresponding to the anatase phase (JCPDS n° 21-1272). Moreover, the TiO₂ crystallite size for GO-NT composites does not change with the addition of GO (Table 2). In particular, neither the reduction procedure nor the GO loading plays a significant role. This result means that the method of elaboration used here does not influence the structural properties of the TiO₂ nanotubes.

Table 2

Band gap energy values and energy levels of calculated conduction band (E_{CB}) and valence band (E_{VB}) (absolute vacuum scale and in parentheses vs NHE); textural properties (BET specific surface area, pore size) and crystallite size as determined by XRD of the GO-NT composites with different loadings of graphene oxide (from 1.0 to 5.0 wt% GO) reduced or not at 200 °C.

| | %GO | E_g (eV) | E_{CB} (eV) | E_{VB} (eV) | S_{BET} ($m^2 g^{-1}$) | Pore size (nm) | TiO ₂ crystallite size (nm) |
|---------------|-----|------------|---------------|---------------|----------------------------|----------------|--|
| NT | 0 | 3.20 | -4.21 (-0.29) | -7.41 (+2.91) | 248 | 7 | 10 |
| 1%GO-NT | 1 | 3.14 | -4.24 (-0.26) | -7.38 (+2.88) | 185 | 17 | 10 |
| 1.5%GO-NT | 1.5 | 3.14 | -4.24 (-0.26) | -7.38 (+2.88) | 160 | 11 | 10 |
| 2%GO-NT | 2 | 3.10 | -4.26 (-0.24) | -7.36 (+2.86) | 169 | 13 | 10 |
| 3%GO-NT | 3 | 3.09 | -4.26 (-0.24) | -7.35 (+2.85) | 145 | 11 | 11 |
| 5%GO-NT | 5 | 3.06 | -4.28 (-0.22) | -7.34 (+2.84) | 187 | 10 | 10 |
| 1%GO-NT-200 | 1 | 3.14 | -4.24 (-0.26) | -7.38 (+2.88) | 190 | 18 | 10 |
| 1.5%GO-NT-200 | 1.5 | 3.14 | -4.24 (-0.26) | -7.38 (+2.88) | 149 | 11 | 12 |
| 2%GO-NT-200 | 2 | 3.02 | -4.30 (-0.20) | -7.32 (+2.82) | 159 | 14 | 11 |
| 3%GO-NT-200 | 3 | 3.00 | -4.31 (-0.19) | -7.31 (+2.81) | 153 | 12 | 11 |
| 5%GO-NT-200 | 5 | 2.96 | -4.33 (-0.17) | -7.29 (+2.79) | 182 | 13 | 11 |

Table 3

Quantitative analysis of GO-NT composites using XPS and elemental analysis.

| Samples | Elemental analysis XPS | | | | | | | | |
|-------------|------------------------|---------|---------|----------|--------------|---------|---------|---------|---------|
| | (C wt%) | C (wt%) | O (wt%) | Ti (wt%) | C/Ti (atom.) | C—C (%) | C—O (%) | C=O (%) | C—O/C—C |
| 1%GO-NT | 0.6 | 14 | 36 | 48 | 1.2 | 36 | 57 | 7 | 1.6 |
| 1%GO-NT-200 | 0.6 | 15 | 35 | 48 | 1.2 | 57 | 33 | 10 | 1.4 |
| 2% GO-NT | 1.0 | 22 | 36 | 40 | 2.2 | 40 | 52 | 8 | 1.3 |
| 5% GO-NT | 2.4 | 26 | 39 | 35 | 3.0 | 45 | 47 | 8 | 1.0 |

XPS studies were also performed to investigate the chemical state of the carbon atoms when GO is added to TiO₂ nanotubes. Different GO loadings were considered going from 1.0 to 5.0 wt% while the reduction process was studied for GO-NT composites with 1.0 wt% GO. Three different contributions were considered at 284.6 eV, 286.5 eV, and at 288.3 eV corresponding to non-oxygenated C=C, C—O (hydroxyls or epoxy) and C=O bonds (carboxylic) respectively [50]. Table 3 reports the relative proportions of the three carbon species for 1% GO-NT, 1% GO-NT-200, 2% GO-NT, and 5% GO-NT. The evolution of the different carbon species for 1% GO-NT before and after reduction confirms the preceding results acquired for GO alone. The reduction process leads to a marked decrease of the proportion of C species related to hydroxyls or epoxy groups and present on the basal planes of graphene. On the opposite, carboxylic groups are not removed at all by the reduction process showing a quite high stability at least after reduction at 200 °C. Moreover, increasing the GO loading for non-reduced GO-NT samples to 2.0 and 5.0 wt% GO leads to a progressive decrease of the main oxygen-containing groups (hydroxyls and epoxy) at the benefit of non-oxygenated C=C species. This result underlines a lower difficulty to reduce GO-NT composites when increasing GO loadings are mixed with NTs before reduction. Finally, the C weight percentage determined by XPS shows values much higher than those determined by elemental analysis (Table 2) showing that graphene oxide is mainly deposited at the outer surface of TiO₂ nanotubes.

TEM images of GO-NT composites with increasing GO loadings of 1.0, 2.0, and 5.0 wt% are presented in Fig. 5. Low magnification images (Fig. 5A and G) shows the presence of large sheets of graphene oxide. High magnification images (Fig. 5B, E, and I) confirm that regardless the GO loading, TiO₂ nanotubes are supported on the graphene oxide layers and keep their original morphology. According to Figs. 5C and I, the diameter of the TiO₂ is about 10–14 nm while the wall thickness is 2–3 nm. Moreover, the TiO₂ nanotubes present lattice fringes with an interlayer d spacing of 0.35 nm corresponding to the (101) plane of anatase. It is worth mentioning that a minor part of the TiO₂ samples also exhibit a nanosheet-like morphology resulting from a non-complete rolling mechanism process (Fig. 5F). Even if isolated nanotubes can be

found dispersed on the graphene oxide sheets (Fig. 5B, C, and E), TiO₂ still presents the tendency to form bundles of nanotubes suggesting that the graphene oxide-TiO₂ interaction remains partly inefficient for redispersing TiO₂ nanotubes. Finally, it should be noted that TiO₂ nanotubes tend to be wrapped into graphene layers particularly at high GO loadings of 2.0 wt% (Fig. 5E) and of 5.0 wt% (Fig. 5I).

To investigate the optical properties of the GO-NT composites, UV-vis absorption spectra were obtained on TiO₂ nanotubes alone, on graphene oxide reduced or not at 200 °C and finally on the series of GO-NT composites reduced or not with increasing GO loadings (from 1.0 to 5.0 wt%). As shown in Fig. S3 (Supplementary Information), TiO₂ nanotubes display a broad absorbance in the UV region due to ligand-to-metal charge transfer processes (LMCT) with an absorption onset at about 395 nm. Graphene oxide shows a small absorbance band at 250 nm corresponding to $\pi-\pi^*$ transition of aromatic C=C bonds [59,60]. Another band around 300 nm is due to n-n* transitions of C=O bonds. Moreover, a significant absorbance extending to the visible region is detected in agreement with the persistence of electron conjugation within the carbon framework of the graphene nanosheets [61]. Finally, a red shift of the absorption onset from 410 to 425 and finally 445 nm is observed with increasing graphene oxide loading respectively of 1.0, 2.0, and 5.0 wt%. On the opposite, the reduction process at 200 °C has no significant effect on the profile of the UV-vis diffuse reflectance curves.

Determination of band gap energy values were therefore carried out using the Kubelka-Munk method and considering indirect band gap transition for TiO₂ in order to determine the influence of the GO loading and of the reduction process on optical properties of the GO-NT composites (Table 2). Results show that up to 1.5 wt% GO, the reduction treatment does not influence band gap energy values. Moreover, the E_g value of 3.14 eV remains close to the one found for TiO₂ nanotubes (3.20 eV) [62]. For GO loadings ≥ 2.0 wt%, slightly smaller band gap energy values are found when reduced graphene oxide is used instead of its non-reduced counterpart at a given GO loading. This slight decrease of the band gap energy values might result from surface states or impurity energy bands due to GO interaction with TiO₂ nanotubes [63]. This result was also ascribed previously to the formation of Ti—O—C chemical bonding

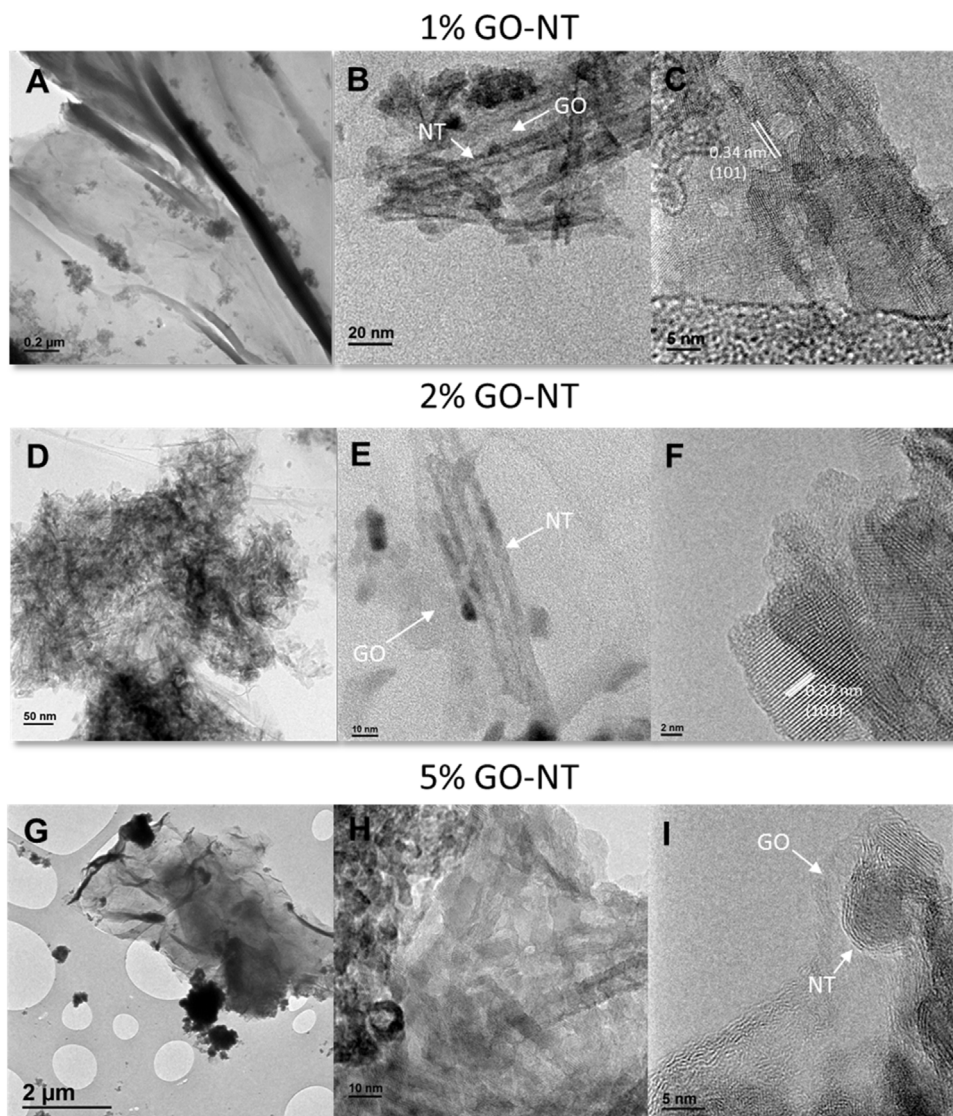


Fig. 5. TEM images of 1% GO-NT: low magnification image showing the presence of graphene layers (A), isolated nanotubes dispersed on graphene oxide (B), and high resolution image of TiO₂ nanotubes (C). TEM images of 2% GO-NT: bundle of TiO₂ nanotubes (D), isolated TiO₂ nanotubes on graphene oxide (E), and high resolution image of non-transformed well-crystallized TiO₂ nanosheets (F). TEM images of 5% GO-NT: low magnification image showing the presence of graphene layers (G), bundles of TiO₂ nanotubes (H), and high resolution image of a single TiO₂ nanotube wrapped with graphene oxide and viewed along its long axis (I).

in carbon-TiO₂ nanocomposites [64,65]. Moreover, conduction and valence band positions were determined considering the following equations (Table 2):

$$Ec(AVS) = -\chi + 0.5Eg$$

$$Ev(AVS) = -\chi - 0.5Eg$$

with χ the electronegativity as given for TiO₂ by Xu et al. [66], Eg the band gap value as determined by UV-vis DRS, AVS = absolute vacuum scale.

The values of Ec and Ev are then also given with respect to the normal hydrogen electrode (NHE) as follows:

$$E(NHE) = -E(AVS) - 4.50.$$

Fig. 6 shows the photoluminescence (PL) spectra of TiO₂ nanotubes alone and of the 1%GO-NT composites before and after reduction of graphene oxide using an excited wavelength at 330 nm. The PL emission spectrum of TiO₂ nanotubes exhibits five main peaks at 408, 446, 459, 486 and 531 nm [67]. The peak at

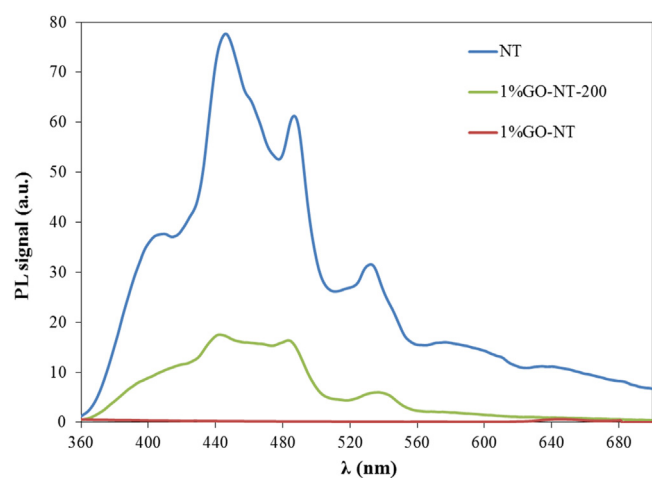


Fig. 6. Photoluminescence spectra of TiO₂ nanotubes (NT) and of 1%GO-NT before and reduction at 200 °C.

Table 4

Relative intensity of the different PL signals for NT and 1%GO-NT-200.

| Samples | Relative Intensity of PL signals (%) | | | | |
|-------------|--------------------------------------|--------|--------|--------|--------|
| | 408 nm | 446 nm | 459 nm | 486 nm | 531 nm |
| NT | 100 | 208 | 176 | 165 | 84 |
| 1%GO-NT-200 | 100 | 189 | 178 | 178 | 78 |

408 nm is due to phonon assisted indirect transition from edge (x) to the center (Γ) of the Brillouin zone [68] while the peak at 446 nm is related to trapped electrons recombining with holes inside the bulk lattice of TiO_2 [69]. Emission peaks at 459 and 531 nm are attributed to recombination of photogenerated electrons with surface oxygen defects [70]. Finally, the emission peak at 486 nm is due to charge transfer from Ti^{3+} to TiO_6^{2-} octahedra [71]. The first point to note when 1.0 wt% GO is added to TiO_2 nanotubes is the complete disappearance of any PL signal for the non-reduced GO-NT composite. This result must be analyzed cautiously. Indeed, TEM results showed that TiO_2 nanotubes are often wrapped with graphene oxide (Fig. 5). GO therefore seems to cover in a large extent the semiconductor surface leading to a shielding effect hiding any useful PL information. Reduction at 200 °C allows retrieving partly some PL signal showing that the reduction treatment leads to a partial uncovering of the semiconductor surface. However, the decreased intensity of the whole PL profile observed in this case cannot be unequivocally assigned to a limitation of the electron-hole recombination [57] since a shielding effect, not related to any recombination phenomenon, can still be effective. Therefore, the only reasonable way to analyze the respective PL profiles of NT and 1%GO-NT-200 is to compare the relative intensities of the different processes occurring (phonon transition, bulk electron-hole recombination, surface recombination with oxygen defects, .) taking into account that only the bulk electron-hole recombination is detrimental to the photocatalytic activity (Table 4). Results show that only the bulk electron-hole recombination at 446 nm present a decreased relative intensity while recombination with surface oxygen defects are not significantly affected. A slight increase of the charge transfer from Ti^{3+} centers can also be noted as expected after reduction. Therefore, a lower bulk electron-hole recombination process can be confirmed on the 1%GO-NT-200 composite showing that graphene oxide can partly limit the recombination of electron-hole pairs.

3.3. Effect of the graphene oxide loading and of the reduction treatment on the photocatalytic properties

Table 5 reports the rate constants for the photodegradation of formic acid using TiO_2 nanotubes alone and GO-NT composites (reduced or not) with increased GO loadings (0.5, 1.0, 1.3, 1.5, 2.0, 3.0, and 5.0 wt%). Rate constants were determined using a methodology developed elsewhere [27]. First, the initial rate (r_0) of degradation was determined at different initial concentrations of formic acid for each photocatalyst. The kinetic behavior was fitted using Langmuir-Hinshelwood formalism. Therefore, the use of the following equation allows the determination of the rate constant k and the adsorption constant K :

$$r_0 = kKC_e/(1 + KC_e)$$

where C_e is the formic acid concentration at the adsorption equilibrium.

Results reported in Table 5 clearly show a beneficial role of GO in enhancing the photocatalytic response of the GO-NT composites. For the case of non-reduced GO, a net increase in photocatalytic activity is observed as soon as 1.0 wt% GO added to TiO_2 nanotubes. Indeed, 1%GO-NT presents a rate constant value k about 40% higher

Table 5

Rate constant (k_{exp}) and adsorption constant (K) values obtained for the photocatalytic degradation of formic acid using NT or GO-NT composite reduced or not and with different loadings (0.5, 1.0, 1.3, 1.5, 2.0, 3.0, and 5.0 wt% GO). Comparison is provided to the P25 reference.

| Catalysts | $k_{\text{exp}} (\mu\text{mol L}^{-1} \text{min}^{-1})$ | $K (10^{-3} \text{ L } \mu\text{mol}^{-1})$ |
|---------------|---|---|
| P25 (ref) | 35 | 20 |
| NT | 73 | 5.9 |
| 0.5%GO-NT | 67 | 1.1 |
| 1%GO-NT | 101 | 1.0 |
| 1.3%GO-NT | 105 | 2.0 |
| 1.5%GO-NT | 107 | 2.0 |
| 2%GO-NT | 57 | 1.6 |
| 3%GO-NT | 54 | 2.9 |
| 5%GO-NT | 54 | 1.0 |
| 0.5%GO-NT-200 | 105 | 1.3 |
| 1%GO-NT-200 | 138 | 0.8 |
| 1.3%GO-NT-200 | 126 | 1.7 |
| 1.5%GO-NT-200 | 123 | 1.9 |
| 2%GO-NT-200 | 69 | 0.8 |
| 3%GO-NT-200 | 58 | 2.4 |
| 5%GO-NT-200 | 53 | 1.9 |

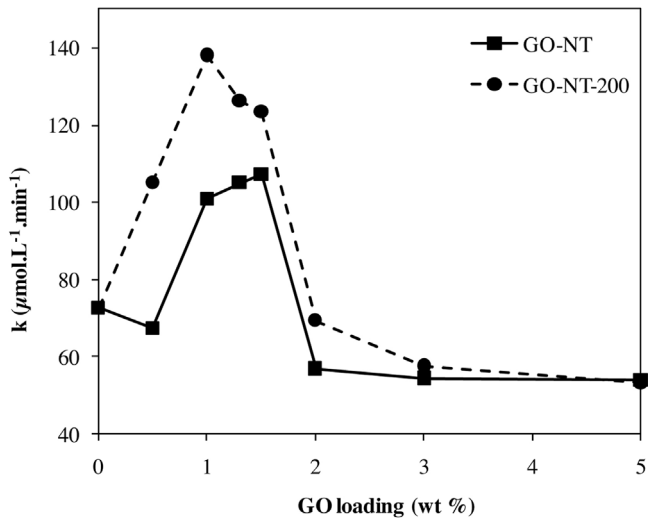


Fig. 7. Comparison of the rate constant values for formic acid photodegradation in function of the GO weight loading for GO-NT photocatalysts reduced or not at 200 °C.

than for the GO-free NT sample (and 190% higher than for the P25 reference). This high photocatalytic response is maintained up to 1.5 wt% GO loading before decreasing as soon as 2.0 wt% GO. For higher loadings of GO, no further decrease in activity can be noticed. The k value obtained in this case is about 25% lower than for NT alone. This lower k value is in agreement with the occurrence of a strong shielding effect of GO as soon as its weight loading reaches 2.0 wt%.

In the case of reduced GO, a similar evolution is observed (Fig. 7) but with a defined maximum activity now centered at 1.0 wt%. Once again, as soon as the GO loading reaches 2.0 wt%, a net decrease in the photocatalytic response is observed. Interestingly, a high gain in photocatalytic activity is reached even at the low GO loading of 0.5 wt% contrary to the non-reduced 0.5 wt% GO-NT composite suggesting that a higher interaction is achieved with TiO_2 when using reduced graphene oxide.

Comparison between reduced and non-reduced graphene oxide shows a beneficial influence of the reduction on the photocatalytic response. The maximum k value observed at 1.0 wt% GO-NT-200 is here 90% higher than for NT alone. Finally, adsorption constant values are systematically smaller on GO-NT composites (reduced or not) than on NT alone.

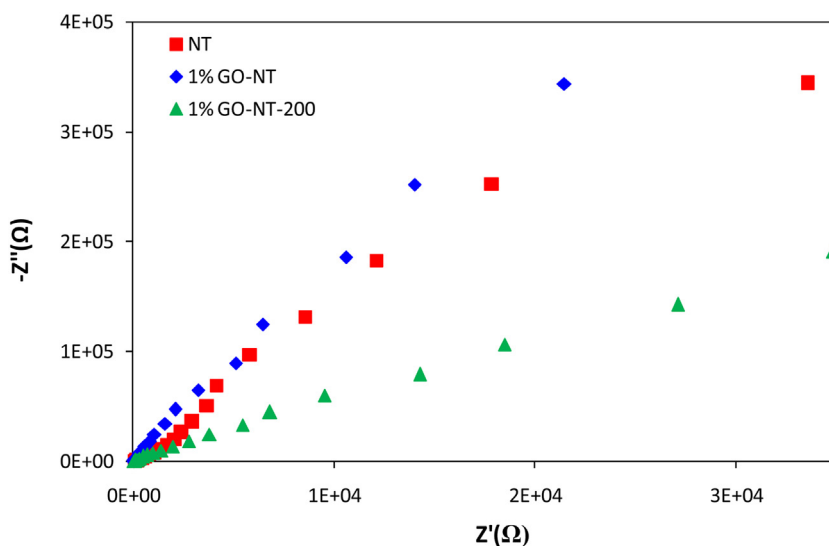


Fig. 8. Nyquist diagrams of NT, 1% GO-NT, and 1% GO-NT-200.

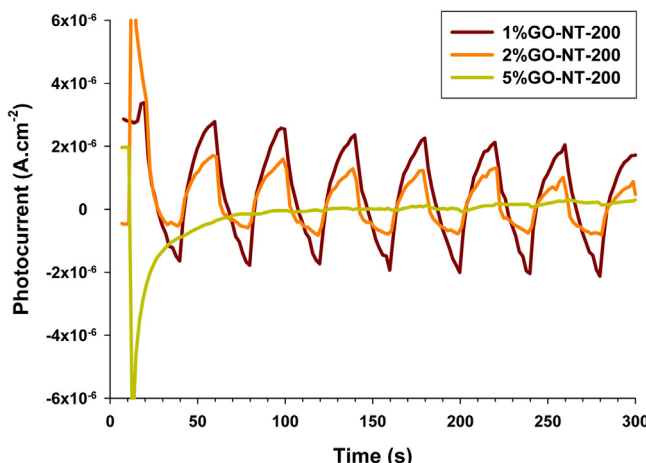


Fig. 9. Photocurrent responses of GO-NT composites reduced at 200 °C with different GO weight loadings (1.0, 2.0, and 5.0 wt%).

The different characterization results acquired here can help to explain such photocatalytic comportment. First, UPS studies have shown that reduced graphene oxide shows a smaller work function and therefore a higher electron affinity than non-reduced graphene oxide showing a direct relationship between the proportion of oxygen-containing groups, their role in the disruption of the π electronic configuration of graphene, and the easiness for transferring photogenerated electrons from the conduction band of TiO₂ to graphene oxide particularly if it is reduced. A second point to be considered is the photoluminescence results of 1% GO-NT-200 which exhibits a lower bulk electron-hole recombination process than for NT alone. Therefore, the easier formation of photoelectrons on the reduced GO-NT composite combined with their higher lifetime can already explain by itself the superiority in terms of photocatalytic response of reduced GO-NT by comparison both to NT and GO-NT. This result is in agreement with previous studies showing that GO and graphene can accept photogenerated electrons from TiO₂ [8,72] leading to a limitation of the electron-hole recombination [9,73–75].

In order to get a deeper understanding of the changes in conductivity of graphene oxide in function of its reduction degree when combined with NTs, complementary electrochemical impedance spectroscopy (EIS) measurements were performed on NT, 1%GO-

Table 6

Impedance results (R_S , R_{CT} , C_{SC} ; see definition of the different parameters in the text) obtained by fitting the experimental data to the equivalent electrical circuit shown in Fig. 9 and evaluation of the electron lifetime at the depletion layer of the semiconductor.

| Photocatalyst | R_S (kΩ) | R_{CT} (MΩ) | C_{SC} (μF) | τ (ms) |
|---------------|------------|---------------|---------------|-------------|
| NT | 42.3 | 3.64 | 43.6 | 159 |
| 1% GO-NT | 41.2 | 2.18 | 28.8 | 63 |
| 1% GO-NT-200 | 43.3 | 1.55 | 24.8 | 38 |

NT, and 1%GO-NT-200 (Fig. 8). Nyquist plots represent the opposite of the imaginary part of the complex impedance as a function of the real part for different values of frequency. Electrical equivalent circuits are determined to explain charge transfer processes occurring in the photoelectrochemical system [76]. The equivalent circuit comprises two distinct contributions: 1) the charge transfer resistance R_{CT} and 2) the space charge capacitance C_{SC} corresponding to the ability of storing charge at the semiconductor/electrolyte interface. As the frequency of the excitation source is increased, the faradaic impedance tends to approach R_{CT} and the Nyquist diagram exhibits a semi-circle. On the opposite, at low frequencies, the faradaic impedance is viewed as a combination of two resistances in series, the first due to electron transfer at the semiconductor/electrolyte interface and the other to mass transport to the electrode, R_S then corresponding to the combined resistances of the glass substrate, of the ionic conductivity of the electrolyte and of the external contact resistance. Results are reported in Table 6. A marked decrease of the charge transfer resistance (R_{CT}) can be noted when going from NT to 1% GO-NT and finally to 1% GO-NT-200, the R_{CT} value for 1% GO-NT-200 being only 42% of the value for NT and 70% of the one for 1% GO-NT. Similarly, the space charge capacitance (C_{SC}) tends to decrease on GO-NT composites but contrary to the R_{CT} evolution, here, the main decrease results from the addition of GO to NT while the reduction process does not influence significantly the charge capacitance. The electron lifetime (τ) at the depletion layer of the semiconductor was calculated based on the following equation [77]:

$$\tau = R_{CT} C_{SC}$$

The electron lifetime decreases sharply when adding graphene oxide to TiO₂ nanotubes, the τ value for 1% GO-NT being only 40% of the one found for NT alone. Reduction of graphene oxide leads to a further decrease of the electron lifetime to only half of the value

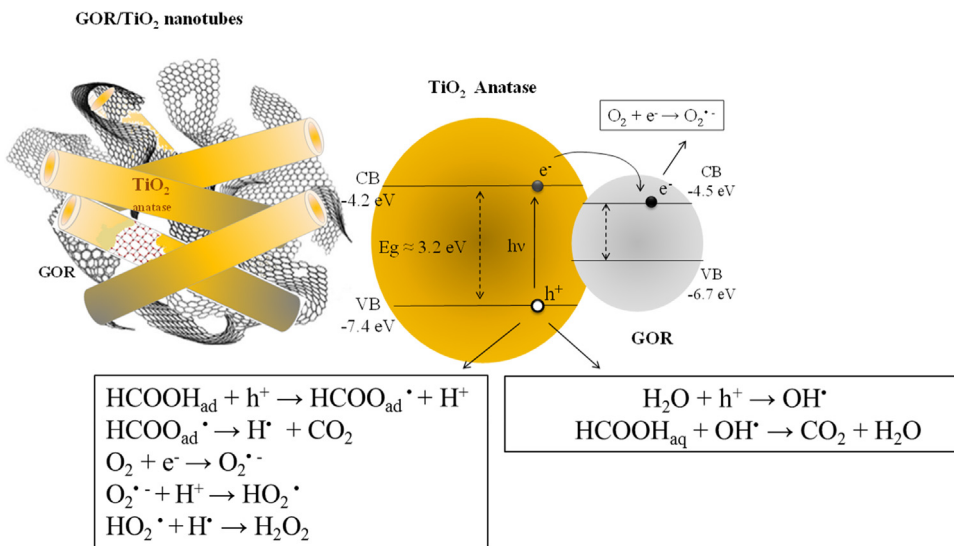
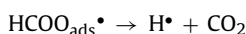
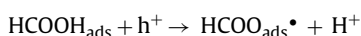


Fig. 10. Schematic diagram of the charge carrier transfer in the GO/TiO₂ nanotube composite under UV irradiation. Main steps occurring during the formic acid photodegradation are also indicated.

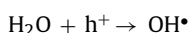
of its equivalent non-reduced counterpart. This decrease is in fact mainly due to the decrease of the charge transfer resistance. Since the probability for an electron to recombine with a hole diminishes with the decrease of the time that this electron spends in the depletion layer at the semiconductor surface, this results means that the recombination of electron-hole pairs is seriously hampered when reduced graphene oxide is added to TiO₂ nanotubes. This also confirms that adding GO leads to a high conductivity of the graphene oxide-NT composite when GO is reduced [78].

Taking into account the superiority of reduced GO-NT composites, the next step is to evaluate why the maximum in photocatalytic activity is reached at a loading of 1.0 wt% of reduced graphene oxide. For this purpose, photocurrent experiments were performed on the series of GO-NT composites reduced at 200 °C with GO loadings of 1.0, 2.0, and 5.0 wt% (Fig. 9). Results clearly evidence a net decrease of the photocurrent intensity as soon as a GO loading of 2.0 wt% while only a featureless response is observed at 5.0 wt%. This suggests a strong shielding effect of reduced graphene oxide which hampers the efficiency of the photocatalytic response at a threshold GO loading value of 2.0 wt%. This effect is also underlined by the lack of stability of the photocurrent response at each cycle since stable intensities are never reached in agreement with a difficulty of light penetration during UV illumination.

The results acquired in this study allows proposing a mechanism explaining the improved performance of the graphene oxide/TiO₂ nanotube composite compared to bare TiO₂ nanotube. Under UV illumination, photogenerated electrons are transferred from the conduction band of TiO₂ anatase nanotubes to graphene oxide (reduced or not) leaving holes available for oxidation reactions increasing the lifetime of photogenerated carriers (Fig. 10). Holes (h⁺) can then react directly with adsorbed formic acid or form OH[•] radicals with formic acid in solution according to the following equations:

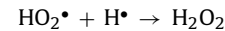
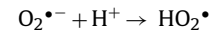


And/or:



Electrons transferred to graphene oxide can then react with $O_2:O_2 + e^- \rightarrow O_2^{\bullet-}$

And the superoxide radicals would then react with H⁺ and H[•] generating H₂O₂ acting also as oxidizing agent for formic acid:



The higher photocatalytic performance observed after reduction of GO can result from a shift of the conduction band of graphene oxide due to a lower work function (as determined by UPS) moving its energy level close to the CB of TiO₂ and therefore improving the transfer of photogenerated electrons as confirmed by EIS measurements.

4. Conclusion

The assembly of GO nanosheets with TiO₂ nanotubes was found to enhance the photocatalytic activity by limiting the recombination rate of photogenerated electron-hole pairs. The addition of GO or reduced GO to TiO₂ nanotubes positively influences the intrinsic performance of titania for formic acid photodegradation. This enhancement of the photocatalytic efficiency is achieved mainly after reduction of the GO-NT nanocomposites under H₂ at 200 °C. Partial reduction of GO improves simultaneously its electron affinity and its electrical conductivity leading to an easier transfer of the photogenerated electrons from the conduction band of TiO₂ to graphene oxide and therefore to successful charge separation. The best photodegradation efficiency of the GO-NT nanocomposites is achieved using only low GO weight loadings (1.0–1.5 wt%). As soon as a threshold GO loading value of 2.0 wt%, strong shielding effect by graphene oxide leads to a depleted photocatalytic response.

Acknowledgements

The authors gratefully acknowledge the financial support by the Tunisian Ministry of Higher Education and Scientific Research and of the French Ministry of Foreign Affairs in the framework of the PHC-Utique program referenced 16G 1202.

Appendix A. Supplementary data

Supplementary data associated with this article can be found, in the online version, at <http://dx.doi.org/10.1016/j.apcatb.2017.02.062>.

References

- [1] D. Robert, S. Malato, *Sci. Total Environ.* 291 (2002) 85–97.
- [2] M. Adachi, Y. Murata, M. Harada, S. Yoshikawa, *Chem. Lett.* 29 (2000) 942–943.
- [3] A. Fujishima, T.N. Rao, D.A. Tryk, *J. Photochem. Photobiol. C* 1 (2000) 1–21.
- [4] H.J. Zhang, P.P. Xu, G.D. Du, Z.W. Chen, K. Oh, D.Y. Pan, Z. Jiao, *Nano Res.* 4 (2011) 274–283.
- [5] S.D. Perera, R.G. Mariano, K. Vu, N. Nour, O. Seitz, Y. Chabal, K.J. Balkus, *ACS Catal.* 2 (2012) 949–956.
- [6] X. Pan, Y. Zhao, S. Liu, C.L. Korzeniewski, S. Wang, Z.Y. Fan, *ACS Appl. Mater. Interfaces* 4 (2012) 3944–3950.
- [7] Y.T. Liang, B.K. Vijayan, K.A. Gray, M.C. Hersam, *Nano Lett.* 11 (2011) 2865–2870.
- [8] W.G. Tu, Y. Zhou, Q. Liu, Z.P. Tian, J. Gao, X.Y. Chen, H.T. Zhang, J.G. Liu, Z.G. Zou, *Adv. Funct. Mater.* 22 (2012) 1215–1221.
- [9] W. Geng, H.X. Liu, X.J. Yao, *Phys. Chem. Chem. Phys.* 15 (2013) 6025–6033.
- [10] H.Q. Sun, S.B. Wang, *Energy Fuels* 28 (2014) 22–36.
- [11] D. Wang, D. Choi, J. Li, Z. Yang, Z. Nie, R. Kou, D. Hu, C. Wang, L.V. Saraf, J. Zhang, I.A. Aksay, J. Liu, *ACS Nano* 3 (2009) 907–914.
- [12] A. Cao, Z. Liu, S. Chu, M. Wu, Z. Ye, Z. Cai, Y. Chang, S. Wang, Q. Gong, Y. Liu, *Adv. Mater.* 22 (2010) 103–106.
- [13] Y.H. Ng, A. Iwase, A. Kudo, R. Amal, *J. Phys. Chem. Lett.* 1 (2010) 2607–2612.
- [14] H. Sun, S. Liu, S. Liu, S. Wang, *Appl. Catal. B* 146 (2014) 162–168.
- [15] Q. Li, B. Guo, J. Yu, J. Ran, B. Zhang, H. Yan, J.R. Gong, *J. Am. Chem. Soc.* 133 (2011) 10878–10884.
- [16] C. Chen, W. Cai, M. Long, B. Zhou, Y. Wu, D. Wu, Y. Feng, *ACS Nano* 4 (2010) 6425–6432.
- [17] J. Liu, L. Liu, H. Bai, Y. Wang, D.D. Sun, *Appl. Catal. B* 106 (2011) 76–82.
- [18] D. Zhao, G. Sheng, C. Chen, X. Wang, *Appl. Catal. B* 111–112 (2012) 303–308.
- [19] W. Wang, J. Yu, Q. Xiang, B. Cheng, *Appl. Catal. B* 119–120 (2012) 109–116.
- [20] W.G. Tu, Y. Zhou, Q. Liu, S.C. Yan, S.S. Bao, X.Y. Wang, M. Xiao, Z.G. Zou, *Adv. Funct. Mater.* 23 (2013) 1743–1749.
- [21] N. Zhang, M.Q. Yang, S.Q. Liu, Y.G. Sun, Y.J. Xu, *Chem. Rev.* 115 (2015) 10307–10377.
- [22] C. Han, N. Zhang, Y.J. Xu, *Nano Today* 11 (2016) 351–372.
- [23] N. Zhang, Y.J. Xu, *CrystEngComm* 18 (2016) 24–37.
- [24] E. Lee, J.Y. Hong, H. Kang, J. Jang, J. Hazard. Mater. 219–220 (2012) 13–18.
- [25] Y. Zhang, Z.R. Tang, X. Fu, Y.J. Xu, *ACS Nano* 4 (2010) 7303–7314.
- [26] F. Zhao, B. Dong, R. Gao, G. Su, W. Liu, L. Shi, C. Xia, L. Cao, *Appl. Surf. Sci.* 351 (2015) 303–308.
- [27] A. Turki, H. Kochkar, C. Guillard, G. Berhault, A. Ghorbel, *Appl. Catal. B* 138–139 (2013) 401–415.
- [28] A. Turki, C. Guillard, F. Dappozze, G. Berhault, Z. Ksibi, H. Kochkar, J. Photochem. Photobiol. A 279 (2014) 8–16.
- [29] A. Turki, H. Kochkar, I. García-Fernández, M.I. Polo-López, A. Ghorbel, C. Guillard, G. Berhault, P. Fernández-Ibáñez, *Catal. Today* 209 (2013) 147–152.
- [30] Y.H. Zhang, Z. Chen, S.Q. Liu, Y.J. Xu, *Appl. Catal. B* 140–141 (2013) 598–607.
- [31] N. Zhang, M.Q. Yang, Z.R. Tang, Y.J. Xu, *ACS Nano* 8 (2014) 623–633.
- [32] K.Q. Lu, N. Zhang, C. Han, F.Y. Li, Z.F. Chen, Y.J. Xu, *J. Phys. Chem. C* 120 (2016) 27091–27103.
- [33] N. Zhang, Y.H. Zhang, Y.J. Xu, *Nanoscale* 4 (2012) 5792–5813.
- [34] M.Q. Yang, C. Han, N. Zhang, Y.J. Xu, *Nanoscale* 7 (2015) 18062–18070.
- [35] M. Mrowetz, E. Sellie, J. Photochem. Photobiol. A 180 (2006) 15–22.
- [36] D.S. Muggli, M.J. Backes, *J. Catal.* 209 (2002) 105–113.
- [37] J. Chen, B. Yao, C. Li, G. Shi, *Carbon* 64 (2013) 225–229.
- [38] D.C. Marcano, D.V. Kosynkin, J.M. Berlin, A. Sinitskii, Z. Sun, A. Slesarev, L.B. Alemany, W. Lu, J.M. Tour, *ACS Nano* 4 (2010) 4806–4814.
- [39] T.D. Dao, H.M. Jeong, *Mater. Res. Bull.* 70 (2015) 651–657.
- [40] M.J. McAllister, J.L. Li, D.H. Adamson, H.C. Schniepp, A.A. Abdala, J. Liu, M. Herrera-Alonso, D.L. Milius, R. Car, R.K. Prud'homme, I.A. Aksay, *Chem. Mater.* 19 (2007) 4396–4404.
- [41] D.S. Sutar, G. Singh, V.D. Botcha, *Appl. Phys. Lett.* 101 (2012) 103103.
- [42] L.M. Pastrana-Martínez, S. Morales-Torres, V. Likodimos, P. Falaras, J.L. Figueiredo, J.L. Faria, A.M.T. Silva, *Appl. Catal. B* 158–159 (2014) 329–340.
- [43] M. Acik, G. Lee, C. Mattevi, A. Pirkle, R.M. Wallace, M. Chhowalla, K. Cho, Y. Chabal, *J. Phys. Chem. C* 115 (2011) 19761–19781.
- [44] M.A. Pimenta, G. Dresselhaus, M.S. Dresselhaus, L.G. Cançado, A. Jorio, R. Saito, *Phys. Chem. Chem. Phys.* 9 (2007) 1276–1290.
- [45] G.K. Ramesha, S. Sampath, *J. Phys. Chem. C* 113 (2009) 7985–7989.
- [46] N.K. Kudin, B. Ozbas, H.C. Schniepp, R.K. Prud'homme, I.A. Aksay, R. Car, *Nano Lett.* 8 (2008) 36–41.
- [47] R.J. Nemanich, S.A. Solin, *Phys. Rev. B: Condens. Matter* 20 (1979) 392–401.
- [48] T. Goksu, R.R. Nair, A. Bonetti, M. Böhmler, A. Lombardo, K.S. Novoselov, A.K. Geim, A.C. Ferrari, A. Hartschuh, *ACS Nano* 3 (2009) 3963–3968.
- [49] A.C. Ferrari, *Solid State Commun.* 143 (2007) 47–57.
- [50] S. Stankovich, R.D. Piner, X. Chen, N. Wu, S.B.T. Nguyen, R.S. Ruoff, *J. Mater. Chem.* 16 (2006) 155–158.
- [51] M.C. Kim, G.S. Hwang, R.S. Ruoff, *J. Chem. Phys.* 131 (2009) 064704.
- [52] S.C. Lim, C.S. Jo, H.J. Jeong, Y.M. Shin, Y.H. Lee, I.A. Samayoa, J. Choi, *Jpn. J. Appl. Phys.* 41 (2002) 5635–5639.
- [53] A. Adan-Mas, D. Wei, *Nanomaterials* 3 (2013) 325–356.
- [54] A. Hunt, E.Z. Kurmaev, A. Moewes, *Carbon* 75 (2014) 366–371.
- [55] H. Ago, T. Kugler, F. Cacialli, W.R. Salaneck, M.S.P. Shaffer, A.H. Windle, R.H. Friend, *J. Phys. Chem. B* 103 (1999) 8116–8121.
- [56] G. Eda, Y.Y. Lin, C. Mattevi, H. Yamaguchi, H.A. Chen, I.S. Chen, C.W. Chen, M. Chhowalla, *Adv. Mater.* 22 (2010) 505–509.
- [57] T.N. Lambert, C.A. Chavez, B. Hernández-Sánchez, P. Lu, N.S. Bell, A. Ambrosini, T. Friedman, T.J. Boyle, D.R. Wheeler, D.L. Huber, *J. Phys. Chem. C* 113 (2009) 19812–19823.
- [58] S. Navalón, A. Dhakshinamoorthy, M. Alvaro, H. Garcia, *Chem. Rev.* 114 (2014) 6179–6212.
- [59] T.D. Nguyen-Phan, V.H. Pham, E.W. Shin, H.D. Pham, S. Kim, J.S. Chung, E.J. Kim, S.H. Hur, *Chem. Eng. J.* 170 (2011) 226–232.
- [60] J.I. Paredes, S. Villar-Rodil, P. Solís-Fernández, A. Martínez-Alonso, J.M.D. Tascon, *Langmuir* 25 (2009) 5957–5968.
- [61] D. Li, M.B. Müller, S. Gilje, R.B. Kaner, G.G. Wallace, *Nat. Nanotechnol.* 3 (2008) 101–105.
- [62] S. Mozia, E. Borowiak-Paleń, J. Przepiórski, B. Grzmil, T. Tsumura, M. Toyoda, J. Grzechulska-Damszel, A.W. Morawski, *J. Phys. Chem. Solids* 71 (2010) 263–272.
- [63] H.Q. Sun, Y. Bai, H.J. Liu, W.Q. Jin, N.P. Xu, G.J. Chen, B.Q. Xu, *J. Phys. Chem. C* 112 (2008) 13304–13309.
- [64] H. Zhang, X. Lv, Y. Li, Y. Wang, J. Li, *ACS Nano* 4 (2010) 380–386.
- [65] W. Ren, Z. Ai, F. Jia, L. Zhang, X. Fan, Z. Zou, *Appl. Catal. B* 69 (2007) 138–144.
- [66] Y. Xu, M.A.A. Schoonen, *Am. Mineral.* 85 (2000) 543.
- [67] M. Meksi, A. Turki, H. Kochkar, L. Bousselmi, C. Guillard, G. Berhault, *Appl. Catal. B* 181 (2016) 651–660.
- [68] N. Serpone, D. Lawless, R. Khairutdinov, *J. Phys. Chem.* 99 (1995) 16646–16654.
- [69] Y. Lei, I.D. Zhang, G.W. Meng, G.H. Li, X.Y. Zhang, C.H. Liang, W. Chen, S.X. Wang, *Appl. Phys. Lett.* 78 (2001) 1125–1127.
- [70] J. Preclíková, P. Galar, F. Trojánek, S. Danis, B. Rezek, I. Gregora, Y. Nemcova, P. Malý, *J. Appl. Phys.* 108 (2010) 113502.
- [71] J. Liu, J. Li, A. Sedhain, J. Lin, H. Jiang, *J. Phys. Chem. C* 112 (2008) 17127–17132.
- [72] X. Wang, H. Tian, Y. Yang, H. Wang, S. Wang, W. Zheng, Y. Liu, *J. Alloys Compd.* 524 (2012) 5–12.
- [73] R. Leary, A. Westwood, *Carbon* 49 (2011) 741–772.
- [74] G. Williams, B. Seger, P.V. Kamat, *ACS Nano* 2 (2008) 1487–1491.
- [75] I.V. Lightcap, T.H. Kosel, P.V. Kamat, *Nano Lett.* 10 (2010) 577–583.
- [76] R. Krishnan, *Fundamentals of semiconductor electrochemistry and photoelectrochemistry*, in: *Encyclopedia of Electrochemistry*, Wiley-VCHVerlag GmbH & Co KGaA, 2007.
- [77] L. Andrade, S.M. Zakeeruddin, M.K. Nazeeruddin, H. Aguilar Ribeiro, A. Mendes, M. Grätzel, *ChemPhysChem* 10 (2009) 1117–1124.
- [78] C. Mattevi, G. Eda, S. Agnoli, S. Miller, K.A. Mkoyan, O. Celik, D. Mastrogiovanni, G. Granozzi, E. Garfunkel, M. Chhowalla, *Adv. Funct. Mater.* 19 (2009) 2577–2583.